efficient tunable long period grating attenuator with an on-fibre heater [4]. This device uses a fibre with a cladding filled with a polymer that has a refractive index that depends strongly on temperature [4]. The position of the transmission dip in this device is nonlinearly related to the temperature and, therefore, the resistance of the coating. These data suggest that a calibration between the transmission dip and the resistance could enable active control of the optical properties. For both the Bragg and the long period devices, applying enough current to the heaters to reach a constant resistance ensures that their operation is insensitive to the ambient temperature (provided that the operating temperature exceeds that of the ambient). It is important to note that this approach to stabilisation does not depend on the exact relationship between the resistance and the optical properties. It does, however, require that (i) variations in temperature along the gratings are small, and (ii) thermally induced changes in the dimensions of the packages for the devices do not significantly affect the properties of the gratings.

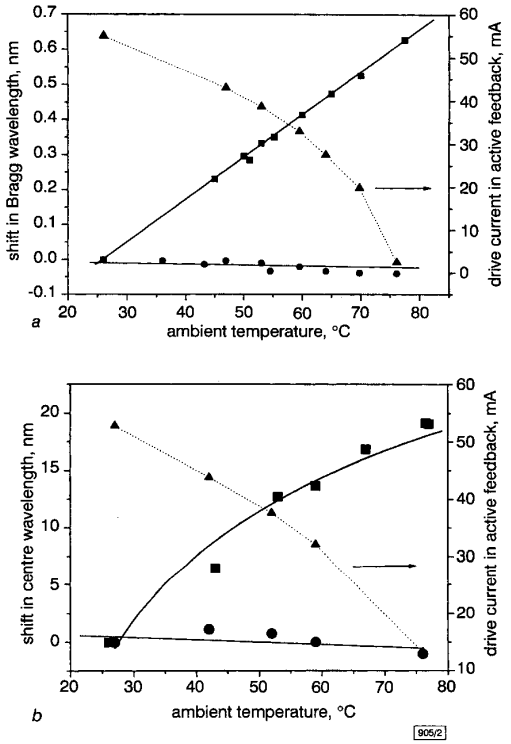

Fig. 2 *Shift in Bragg wavelength against ambient temperature when constant current is supplied to thin-film on-fibre heater and device is operated with sufficient current to maintain constant value of heater resistance and similar data collected for power-efficient thermally actuated long-period grating*

a Shift in Bragg wavelength against ambient temperature
b Data for power-efficient actuated long-period grating
■ wavelength shift with constant current supplied to thin-film on-fibre heater
● wavelength shift with sufficient current to maintain constant value of heater resistance
▲ current required to maintain constant resistance
Lines are guides to eye

Results and discussion: Fig. 2 illustrates the results of active temperature stabilised operation of thermally tuned Bragg and long period gratings that use distributed on-fibre resistive heaters. In both cases, a power supply delivers a known current to the devices and, their resistance is measured. The current is adjusted every ~1–10s (slightly longer than the response times of the devices) to maintain a fixed, user-defined resistance. Fig. 2 also shows the variation of the applied current as the device is operated, at constant resistance, in an oven heated to various temperatures. The data show that this form of electrical feedback effectively stabilises the optical characteristics against ambient temperature variations. In fact, constant resistance operation reduces the temperature sensitivity of both types of devices by more than an order of magnitude when compared with operation at constant current (also shown in Fig. 2). These results are comparable to those for packages designed to temperature compensate for the properties of static Bragg and long period grating devices [8].

Conclusions: We have demonstrated a scheme for using distributed thin film on-fibre heaters simultaneously as temperature sensors for stabilised operation of thermally actuated grating devices. Like many other methods for temperature stabilisation or compensation, the technique is most effective when variations in the temperature along the grating can be neglected. Also, in the absence of a means to cool the devices, the lowest operating temperature must exceed the highest expected ambient temperature. Nevertheless, the approach is simple, it works well and it does not require any modification to the design of the devices. Finally, although the devices described in this Letter rely on heaters with a resistance that changes linearly with temperature, it is important to note that the resistance only needs to exhibit a monotonic variation with temperature in order for the approach to be effective.

13 October 1999
Electronics Letters Online No: 19991381
DOI: 10.1049/el:19991381

J.A. Rogers, B.J. Eggleton and P. Kuo (*Bell Laboratories, Lucent Technologies, 600 Mountain Avenue, Murray Hill, NJ 07974, USA*)

References

1 ROGERS, J.A., *et al.*: 'Distributed on-fiber thin film heaters for Bragg gratings with adjustable chirp', *Appl. Phys. Lett.*, 1999, **74**, pp. 3131–3133
2 ROGERS, J.A., *et al.*: 'Dual on-fiber thin-film heaters for fiber gratings with independently adjustable chirp and wavelength', to be published in *Opt. Lett.*
3 LIMBERGER, H.G., *et al.*: 'Efficient miniature fiber-optic tunable filter based on intracore Bragg grating and electrically resistive coating', *IEEE Photonics Technol. Lett.*, 1998, **10**, pp. 361–363
4 ABRAMOV, A.A., *et al.*: 'Electrically tunable efficient broadband filter', *IEEE Photonics Technol. Lett.*, 1999, **11**, pp. 445–447
5 EGGLETON, B.J., *et al.*: 'Dispersion compensation in a dynamic 20Gbit/s nonlinear lightwave system using electrically tunable chirped fibre grating', *Electron. Lett.*, 1999, **35**, pp. 832–833
6 NIELSEN, T., *et al.*: 'Fiber Bragg grating tunable dispersion compensator for dynamic post dispersion optimization at 40Gb/s', *IEEE Photonics Technol. Lett.*,
7 'CRC handbook of chemistry and physics'. 66th edn., E-88, 1985
8 YOFFE, G.W., *et al.*: 'Passive temperature-compensating package for optical fiber gratings', *Appl. Opt.*, 1995, **34**, pp. 6859–6861

Single acquisition polarisation imaging with digital holography

D. Beghuin, E. Cuche, P. Dahlgren, C. Depeursinge, G. Delacrétaz and R.P. Salathé

A demonstration of the ability of digital holography to image and to measure spatial variations of the polarisation of an object wave with a single image acquisition is presented. This is achieved by recording a hologram with two reference beams presenting orthogonal polarisations and different propagation directions. A CCD camera is used to record the hologram and the reconstruction is performed numerically.

Introduction: Polarisation imaging has long been recognised as being useful for revealing the inner structures or stresses of numerous materials (biological, among others). The use of holography for polarisation imaging was proposed by Lohmann [1]. However, the cumbersome handling of classical substrates for hologram recording has hindered the practical use of the technique. In [2, 3] a new attractive method of digital holography was presented in which a hologram recorded with a CCD camera is numerically reconstructed. We demonstrate in this Letter, using the configuration proposed by Lohmann, that digital holography can be used to image and to measure the spatial distributions of two components of the Stokes vector at the surface of the specimen. In comparison with other techniques for polarisation measurements, the

presented technique has the unique feature of requiring a single image acquisition stage.

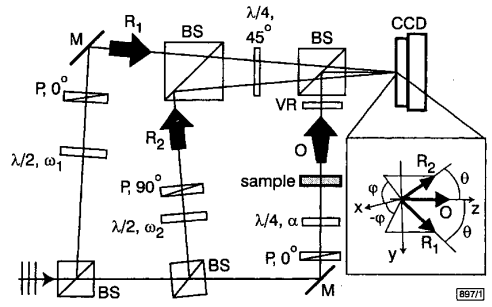

Fig. 1 *Experimental setup*

M: mirror; P: polariser; BS: beam splitter; λ/4: quarter wave plate; λ/2: half wave plate; VR: variable retarder

Method: The configuration used for hologram recording is presented in Fig. 1. It consists of a modified Mach-Zehnder interferometer with two reference waves $\mathbf{R}_1$ and $\mathbf{R}_2$. We use a plane wave output from a CW Nd:YAG laser (1064nm) to generate the three interfering waves ($\mathbf{R}_1$, $\mathbf{R}_2$, and $\mathbf{O}$). In each reference arm, a polariser (P) and a half-wave plate (λ/2) are used to control the polarisation and the intensity of the reference waves. The polarisers are oriented to obtain vertical and horizontal polarisations for $\mathbf{R}_1$ and $\mathbf{R}_2$, respectively, and the orientation of the fast axes of the two λ/2 (ω_1 and ω_2) are adjusted to equalise the intensities of $\mathbf{R}_1$ and $\mathbf{R}_2$. The references then recombine and pass through a quarter-wave plate (λ/4) at 45° that transforms the polarisations to be circularly right and circularly left handed.

The hologram is recorded in an off-axis geometry with the three waves propagating along different directions. As shown inset in Fig. 1, the object wave $\mathbf{O}$ has a normal incidence (along $0z$) on the CCD plane $0xy$. $\mathbf{R}_1$ and $\mathbf{R}_2$ propagate symmetrically with respect to the $0xz$ plane and have the same incidence angle (θ) with respect to $0z$. Experiments presented here have been performed with $\theta = 2{,}15°$ and azimuth angles $\varphi = \pm 45°$. The polarisation of the beam illuminating the object is controlled by a quarter wave plate (λ/4) the fast axis of which forms an angle α with the axis of the vertical polariser (P). The object wave $\mathbf{O}$ is directed towards the CCD by a beam splitter (BS). The undesired phase shift between horizontal and vertical components of the polarisation that is induced by reflection on the BS is cancelled out by a properly adjusted liquid crystal variable retarder (VR).

The interference between $\mathbf{R}_1$, $\mathbf{R}_2$ and $\mathbf{O}$ produces the hologram. As $\mathbf{R}_1$ and $\mathbf{R}_2$ have orthogonal polarisations, they do not interfere ($\mathbf{R}_1\mathbf{R}_2^* = \mathbf{R}_1^*\mathbf{R}_2 = 0$) and the hologram intensity is

$$I_H = |\mathbf{O}|^2 + |\mathbf{R}_1|^2 + |\mathbf{R}_2|^2 + \mathbf{R}_1\mathbf{O}^* + \mathbf{R}_2\mathbf{O}^* + \mathbf{O}\mathbf{R}_1^* + \mathbf{O}\mathbf{R}_2^* \quad (1)$$

The numerical reconstruction of the hologram is performed in the Fresnel approximation. The distribution of intensity $I(m, n)$ in the reconstruction plane is obtained using the following algorithm [3]:

$$I(m,n) = \left| DFT\left[I_H(k,l) \exp\left\{ \frac{i\pi}{\lambda d}\left[(k\Delta x)^2 + (l\Delta y)^2\right]\right\}\right]_{m,n} \right|^2 \quad (2)$$

where k, l, m, n are integers, DFT is the discrete Fourier transform operator, λ is the wavelength and d represents the distance at which the Fresnel diffraction is evaluated. With a personal computer, a reconstruction rate of about two reconstructions per second can be achieved for 512 × 512 pixels. During the reconstruction, the first three terms of eqn. 1 generate a zero order of diffraction. The fourth and fifth terms produce two real images corresponding to the orthogonal polarisations and the two last terms produce their so-called twin images. Since the hologram is recorded in an off-axis geometry, these different terms appear at different locations in the reconstructed image.

Assume that $\mathbf{v}_1$ and $\mathbf{v}_2$ are the normalised orthogonal states of polarisation with $\mathbf{R}_1 = R_1\mathbf{v}_1$ and $\mathbf{R}_2 = R_2\mathbf{v}_2$ (R_1 and R_2 being complex). The diffracted object wave can then be decomposed along $\mathbf{v}_1$ and $\mathbf{v}_2$: $\mathbf{O} = O_1\mathbf{v}_1 + O_2\mathbf{v}_2$, ($O_1$ and O_2 being complex). The real image terms in eqn. 1 then become

$$\mathbf{R}_1\mathbf{O}^* = R_1\mathbf{v}_1(O_1^*\mathbf{v}_1 + O_2^*\mathbf{v}_2) = R_1O_1^* \quad (3)$$

$$\mathbf{R}_2\mathbf{O}^* = R_2\mathbf{v}_2(O_1^*\mathbf{v}_1 + O_2^*\mathbf{v}_2) = R_2O_2^* \quad (4)$$

and their intensities $|R_1O_1|^2$ and $|R_2O_2|^2$ are proportional to $|O_1|^2$ and $|O_2|^2$ ($|R_1|^2$ and $|R_2|^2$ are constants). While $|O_1|^2$ and $|O_2|^2$ are usually recorded separately, here they are obtained in a single operation due to their spatial separation in the reconstruction plane. Depending on the choice of $\mathbf{v}_1$ and $\mathbf{v}_2$ it is possible to compute the distribution of the Stokes vector components S_0 and S_1, S_2 or S_3. The S_0 and S_3 components are obtained by summing and subtracting the intensities of the two reconstructed images, choosing $\mathbf{R}_1$ and $\mathbf{R}_2$ with right circular and left circular polarisation, respectively. The S_1 and S_2 components can be obtained in the same manner recording the hologram with the corresponding polarisation states.

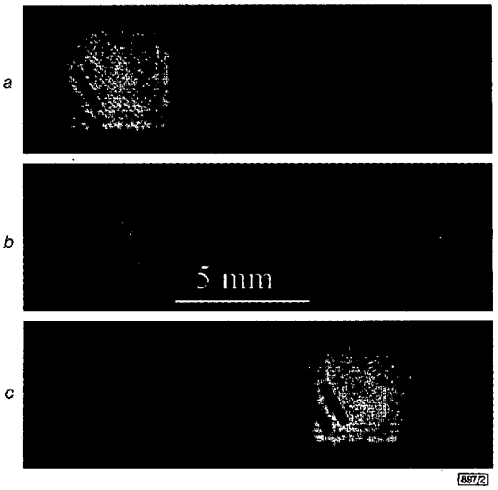

Fig. 2 *Reconstructed images of USAF test target for three polarisations of object wave*

a Left circular (α = –45°)
b Linear vertical (α = 0°)
c Right circular (α = +45°)

Results: The negative USAF target used as the object is composed of a glass plate on which absorbing elements in the form of three bar patterns have been created. The polarisation of the object wave is varied by changing the angle α of the λ/4. The images reconstructed for three different values of α (–45°, 0° and 45°) are shown in Fig. 2*a–c*, respectively. Only the real images are represented; the zero order and twin images are removed for the sake of clarity. In Fig. 2*b*, the polarisation of $\mathbf{O}$ is vertical and decomposes therefore equally along the two orthogonal polarisation states (right circular and left circular). In Fig. 2*a* and *c*, the polarisation of $\mathbf{O}$ is right circular and left circular, respectively, and interference only occurs with the corresponding reference waves. Preliminary experiments have shown that quantitative values can be obtained for elliptical polarisation (intermediate α values).

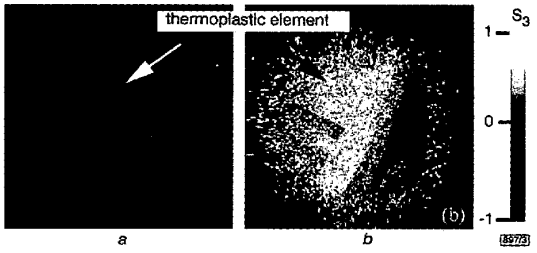

Fig. 3 *USAF test target partially covered by birefringent thermoplastic material*

a Total intensity S_0
b Normalised S_3 Stokes component

The ability of the method to image spatial variations of the polarisation is demonstrated in Fig. 3. For this purpose, a thermoplastic element is used to cover part of the USAF test target. The obtained distribution for the S_0 (i.e. the intensity) and S_3 components are presented in Fig. 3*a* and *b*, respectively. The zone of the object that is not covered by the thermoplastic element does not modify the vertical polarisation ($S_3 = 0$), while the thermoplastic material turns the polarisation to right circular ($S_3 = 1$). Noise appears in Fig. 3*b*, where the total intensity is weak, e.g. at the border of the thermoplastic element or in the bar patterns of the test target.

Conclusion: The results presented here demonstrate that mapping of the polarising properties of a sample can be achieved by numerical reconstruction of a hologram recorded with two reference waves presenting distinct propagation directions and orthogonal polarisation states. The acquisition realised with a single camera is fast (25Hz) and can be applied to study transient processes. The polarisation information adds to the intensity and phase distributions [3] that are also available from the hologram, providing a complete description of the optical field at the surface of the specimen.

Acknowledgments: This work was supported by the Swiss National Fund for Scientific Research grant 20-49628.96 and by the Swiss Priority Program 'Optical Sciences, Applications and Technologies'.

13 October 1999
Electronics Letters Online No: 19991377
DOI: 10.1049/el:19991377

D. Beghuin, E. Cuche, P. Dahlgren, C. Depeursinge, G. Delacrétaz and R.P. Salathé (*Institut d'Optique Appliquée, Ecole Polytechnique Fédérale de Lausanne, CH-1015 Lausanne, Switzerland*)

E-mail: didier.beghuin@epfl.ch

References

1 LOHMANN, A.W.: 'Reconstruction of vectorial wavefronts', *Appl. Opt.*, 1965, **4**, pp. 1667–1668
2 SCHNARS, U.: 'Direct phase determination in hologram interferometry with use of digitally recorded holograms', *J. Opt. Soc. Am. A*, 1994, **11**, pp. 2011–2015
3 CUCHE, E., BEVILACQUA, F., and DEPEURSINGE, C.: 'Digital holography for quantitative phase-contrast imaging', *Opt. Lett.*, 1999, **24**, pp. 291–293

Near and middle infrared dual band operation of InGaAs/InP quantum well infrared photodetector

H.C. Liu, Chun-ying Song, E. Dupont, P. Poole, P.H. Wilson, B.J. Robinson and D.A. Thompson

An investigation is presented into the dual band operation of an InGaAs/InP quantum well infrared photodetector for both near and middle infrared spectra. The detector performance is evaluated and analysed. It is found that such devices are potentially useful for applications involving dual band simultaneous detection and imaging.

The quantum well infrared photodetector (QWIP) [1] is a well known device. This, together with other devices using intersubband transitions in quantum wells, represents a successful use of low dimensional quantum structures in practical applications [2]. In this Letter we report on the dual band operation of an InGaAs/InP QWIP for both near infrared (NIR) and middle infrared (MIR) spectra. The need in applications for multi-spectral sensors motivated us to pursue investigating the use of dual band devices. The idea of dual band operation of an InGaAs/InP QWIP is straightforward. A regular QWIP structure with InGaAs wells and InP barriers is used for MIR detection [3]. At the same time, NIR can be absorbed in the InGaAs layers resulting in a photocurrent. The contact layers of the QWIP are made of InP so that the NIR light can reach the quantum well region without being absorbed. In this Letter, we present the experimental results of an InGaAs/InP QWIP and analyse its performance.

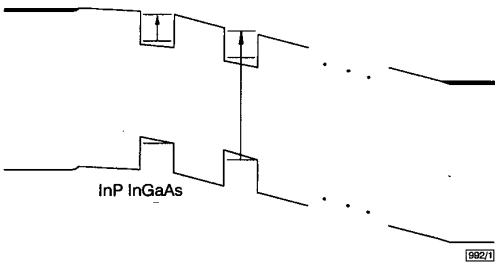

Fig. 1 *Schematic band-edge profile of device*

Arrow within conduction band quantum well shows detection process for middle infrared, while arrow from valence band to conduction band indicates excitation of electrons by near infrared

The test device that we used for this proof-of-concept experiment was an 8 well InGaAs/InP QWIP grown on a semi-insulating InP substrate. The InGaAs wells and the InP barriers were ~7.3 and 27nm thick, respectively. The wells were doped with Si to $10^{18}cm^{-3}$. The barriers next to the top and bottom contact layers were 54nm thick. The InP contact layers were doped with Si to $10^{18}cm^{-3}$. The band-edge profile of the device is schematically shown in Fig. 1. Mesa devices 120×120 and $240 \times 240\mu m^2$ in size were made. A 45° edge facet was polished for light coupling to the intersubband transition [4]. The packaged device was mounted in a liquid nitrogen dewar. A Bomem DA8 Fourier transform spectrometer was used for photoresponse spectral measurements. For the MIR region a KBr beamsplitter and a glowbar source were used, while for the NIR region a quartz beamsplitter and a quartz-halogen source were employed. The calibration for the MIR regions was performed using a 1000K blackbody source and a variable narrowband filter. An Nd-YAG laser at 1.06μm was used for the NIR responsivity calibration. The spectral photoresponse curves for both MIR and NIR regions are shown in Fig. 2. Clearly, the device is indeed working as a dual band detector. All features in the curves can be accounted for by considering the confined conduction and valence quantum well states, labelled E1 and E2 for the conduction states, HH1 and HH2 for the heavy hole valence band, and LH1 and LH2 for the light hole valence band. The difference between E1 and E2 corresponds to the MIR peak. The interband process is slightly more complicated as several transitions are allowed. The transitions involving HH1 or LH1 to E1 should give rise to a small photocurrent since the photoexcited carriers are likely to recombine in the same well before escaping. Transitions from HH2 or LH2 to E2 should give a strong contribution because the photoexcited electrons should escape in a shorter time scale than the relaxation time. All possible transitions are shown in Fig. 2. A clear correspondence is seen. The sharp cutoff at 1.4eV is due to the InP substrate absorption since the light must pass through the substrate after entering the 45° facet.

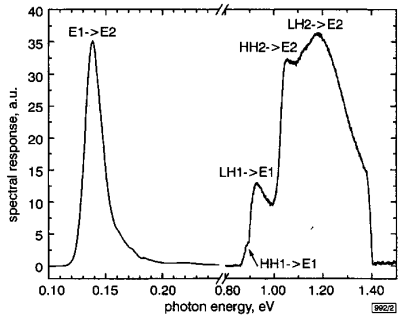

Fig. 2 *Spectral photoresponse curves at device temperature of ~80K*

Data were taken with two different sets of beamsplitters and sources; the two parts are separately normalised